Numerical Study of Solid Particle Erosion on the Tubes Near the Side Walls in a Duct with Flow Past an Aligned Tube Bank

Zeli Wang, Jianren Fan, and Kun Luo
State Key Laboratory of Clean Energy Utilization, Zhejiang University, Hangzhou 310027, P. R. China

DOI 10.1002/aic.11971
Published online August 11, 2009 in Wiley InterScience (www.interscience.wiley.com)

Computational fluid dynamic (CFD) tool has been applied to investigate the erosion of duct walls and that of tubers (10 × 10 aligned tube bank in the duct) near side walls, which is caused by coal ash particle impaction. The flow field is obtained by using direct numerical simulation (DNS) method. The coupling between tubes and flows are made through the immersed boundary technique. Particles are tracked by using Lagrangian approach and further coupled with gas phase. Four coal ash particles are considered 6.2, 20, 80, and 200 μm. In the end, the erosion of the duct walls and that of the tubes near side walls has been well predicted and characterized.
 AIChE J, 56: 66–78, 2010
Keywords: aligned tube bank erosion, immersed boundary method, direct numerical simulation

Introduction

Many industrial applications such as chemical plants, coal combustion equipments, and heat exchangers encounter serious problems from the tube erosion in tube banks caused by particle impacts. Many researchers have investigated the mechanism of erosion experimentally. Finnie[1] studied the wear of a surface due to solid particle erosion and pointed out that the influences of particle velocity and angle in the erosion of a brittle material and a ductile material are quite different. Tabakoff et al.[2] studied the erosion of different alloy by coal ash particles experimentally and showed the methods of predicating erosion damage in material exposed to coal ash. Laitone[3] investigated the velocity effects on the erosion of a ductile material by aerodynamically entrained solid particles experimentally and indicated that erosion varied with the fourth power of velocity in normal impacts. Sundararajan[4] proposed an empirical equation relating the volume of the crater formed during high velocity oblique impact tests to the velocity and angle of impact and to the target material hardness. Deng et al.[5] studied the influence of particle spin on the solid particle erosion rate of metals and indicated that a strong effect of the spin direction on erosion rate at low impact angles when the targets were impacted by angular particles.

With the development of computational fluid dynamics (CFD), numerical study becomes a useful tool for the prediction of material erosion due to solid particle impacts. There are two approaches to predict wear caused by solid particles on the surface of a material. One is Eulerian approach where the particulate phase is treated as a continuum and the trajectory of each particle is not tracked. Using this method, Lee et al.[6] predicted the solid particle erosion for a single tube in a cross flow. Another method is Lagrangian approach where particulate phase is treated as discrete particle and each particle is calculated at every time step so the detail of the solid particle erosion can be obtained. On the basis of Lagrangian approach, Fan et al.[7] developed a stochastic particle dispersion model to investigate the coal particle dynamics about a tube. The erosion damage of the tube is proportional to the free stream velocity to the power 3.30–3.78 and the maximum erosion damage occurs for the tube angle in the range 40°–50°. Sato et al.[8] studied the erosion rate of wall surfaces for a gas–solid suspension flowing in a duct by using the

Correspondence concerning this article should be addressed to J. Fan fanjr@zju.edu.cn

Eulerican description for the fluid flow and the Lagrangian description for the particulate phase. Wallace et al.[9] used the Lagrangian method to track the trajectories of particles with empirically developed equations of the mass removal to examine erosion in valve components for aqueous slurry flows. Fan et al.[10] studied a finned tube erosion protection method numerically and experimentally and indicated that the fin relative height, the fin number, and the angle between two adjacent fins are important parameters in these finned tube erosion protection abilities. Song et al.[11] investigated a method to reduce erosion by adding ribs to the wall of a duct contain a particulate two-phase flow numerically. Fan et al.[12] used the large eddy method for obtaining the flow field and applied the Lagrangian approach for getting track particle trajectories and then achieved the antierosion characteristics of the ribbed-bend in gas–solid flows. The erosion rate of all the ribbed bends were greatly reduced compared with that of the bare bend. Mbabazi et al.[13] tested the accuracy of an erosion model in predicting the erosion by fly ash of air heater elements by comparing the results obtained by the CFD simulations with the results obtained in experimental investigations. They found that augmentation the turbulence of the gas–particle flow might increase the frequency of particle–wall collisions.

The accuracy of wear prediction depends on three aspects: the accuracy of computing the flow field, the accuracy of tracking the trajectories of particles and the rationality of erosion model. In terms of computing the flow field, the k-ε turbulence model is a basic and efficient method to calculate the fluid phase turbulent as well as considering particulate erosion problems.[6–11,13] Large eddy method is more accurate than the k-ε turbulence model for computing the flow field, which can also be applied in wear prediction.[12] As the most accurate method, direct numerical method solves the Navier–Stokes equations directly without any closure model in predicting the gas flow field. To track the trajectories of particles, both the Eulerian and the Lagrangian approach are available. The Eulerian approach to calculate the particle velocity field is economical in time[6] while the Lagrangian approach can get the full information about the particulate movement such as each particle's position and velocity during the whole computing time. Many researchers have done a lot of experimental tests and proposed many erosion models for different applications.[1–5] A reasonable erosion model in combination with a CFD tool can obtain accurate prediction for solid particle erosion of surfaces. The direct numerical simulation method with Lagrangian particle tracking has been applied to solve some practical problems. Sbrizzai et al.[14] applied this method to study the turbulent particle dispersion in an unbaffled stirred-tank reactor. Gradl et al.[15] used this method with the population balance and micromixing model to predict the particle size distribution in nanoparticle precipitation. However, the direct numerical simulation method with Lagrangian particle tracking has been seldom applied to the erosion prediction.

When applying the CFD tool to predict the erosion of tube banks, one challenge is to calculate the complex flow field accurately. In the work of Fan et al.[7] and Schuh et al.,[16] a simply flow domain is applied with a periodic boundary condition in the transverse direction. This kind of consideration is suitable when there is no vortex shedding from the tubes in low Reynolds number flow. However, in most industrial practices, the vortex sheds from tubes will affect the flow field, the movement of particle and the magnitude of erosion. Therefore, it is necessary to compute the whole domain to study the solid particle erosion of a tube bank. Grid generation and coordinate transformation is another problem in computing a complex flow field. To prevent the complex curvilinear coordinate generation, the immersed boundary technique,[17–19] which is based on a Cartesian grid structure can be used to handle this kind of complex geometry.

In many industrial applications, tubes near a wall suffered serious erosion caused by particles impingement. In the present work, coal ash particles wear the side walls and the tubes near side walls of a duct are investigated numerically when these particles follow a cross flow past an 10×10 aligned tube bank in the duct. The flow field is obtained through direct numerical simulation, the coupling between tubes and flows are done through the immersed boundary technique and the trajectories of particles are tracked by a Lagrangian approach with a two-way coupling method. From the computed results, we will predict the most severe erosion damage positions on the side walls and on the tubes near side wall of the pipe, which is very helpful for reducing erosion.

Numerical Method

Solution domain

Figure 1 shows the schematic view of the whole computational domain. The aligned tube bank contains 10×10 tubes with diameter $D = 30$ mm. The dimensions of computational duct are $L_x = 29D$ in streamwise direction and $L_y = 21D$ in transverse direction. The distance between tubes in transverse and longitudinal direction is equal to $2D$. The center of the first transverse row of tubes in streamwise direction is located at $4.5D$. And the distance between the center of the first row of tubes in transverse direction and the wall of pipe is $2D$. The tubes masked by dashed line and numbered near the up side wall in Figure 1 and two side walls are the investigated objects in present work.

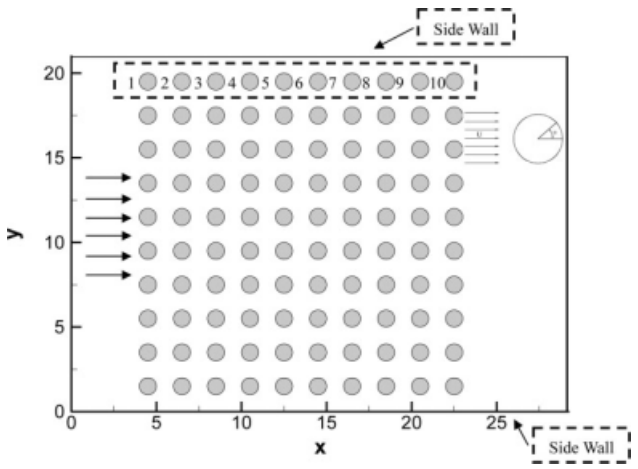

Figure 1. Schematic view of the computational domain.

Governing equations for gas-phase flow

The dimensionless governing equations for incompressible viscous flows in the entire computational domain are:

$$\nabla \cdot \boldsymbol{u} = 0 \tag{1}$$

$$\frac{\partial \boldsymbol{u}}{\partial t} + \boldsymbol{u} \cdot \nabla \boldsymbol{u} = -\nabla P + \frac{1}{\mathrm{Re}} \nabla^2 \boldsymbol{u} + f_\mathrm{d} + f \tag{2}$$

where $\boldsymbol{u}$ is the velocity of fluid, P is the pressure and Re is the Reynolds number defined as $\mathrm{Re} = \frac{\rho_f \cdot \tilde{U} \cdot \tilde{L}}{\mu}$. Here ρ_f is the density of fluid, $\tilde{U}$ is the characteristic velocity of flow field, $\tilde{L}$ is the characteristic length of flow field, and μ is the viscosity of fluid. f_d is the coupling term between the fluid and the discrete particles. f in Eq. (2) is the external force exerted on the flow field which is the mutual interaction force between fluid and immersed boundary expressed as following formulation:

$$f(\boldsymbol{x}) = \int_\Omega \boldsymbol{F}_\mathrm{k}(\boldsymbol{x}_\mathrm{k}) \cdot \delta(\boldsymbol{x} - \boldsymbol{x}_\mathrm{k}) d\boldsymbol{x}_\mathrm{k} \tag{3}$$

where $\delta(\boldsymbol{x} - \boldsymbol{x}_\mathrm{k})$ is the Dirac delta function, $\boldsymbol{x}_\mathrm{k}$ is the position of the Lagrangian points set at the immersed boundary, $\boldsymbol{x}$ is position of the computational Eulerian mesh, and $\boldsymbol{F}_\mathrm{k}(\boldsymbol{x}_\mathrm{k})$ is the force exerted on the Lagrangian point $\boldsymbol{x}_\mathrm{k}$.

To solve the governing equations, the spatial derivatives are discretized using the fourth order compact finite difference scheme[20] based on a nonstaggered grid. The pressure-Poisson equation derived by applying the divergence operator to the momentum equations replaces the continuity equation, which is indirectly satisfied with the solution of the pressure equation. To reduce the cost of memory in simulations, a four-step-four-order marching scheme[21] is applied to the time integration. The no-slip boundary condition is applied at two side walls of the duct. The no-reflect velocity boundary condition (Eq. 4) is used at the outflow boundary.[22]

$$\frac{\partial \boldsymbol{u}}{\partial t} + c \frac{\partial \boldsymbol{u}}{\partial x} = 0 \tag{4}$$

where c is the mean velocity at the outflow boundary.[23]

Lagrangian formulation for particles

The trajectories of solid particles are tracked by the Lagrangian approach with two-way coupling between the gas phase and the particle phase. The interparticle collision and particle rotation are ignored due to the particle phase being considered as a dilute phase. The dimensionless governing equation for a single particle is:

$$\frac{d\boldsymbol{V}}{dt} = \frac{f_\mathrm{p}}{St}(\boldsymbol{u} - \boldsymbol{V}) + \boldsymbol{g} \tag{5}$$

where $\boldsymbol{V}$ are the instantaneous velocity of the particle. $f_\mathrm{p} = 1 + 0.15\ \mathrm{Re}_\mathrm{p}^{0.687}$, Re_p is the particle Reynolds number which takes the diameter of particle as the characteristic length. St is the Stokes number defined as $\mathrm{St} = \frac{\rho_\mathrm{p} d_\mathrm{p}^2/(18\mu)}{\tilde{L}/\tilde{U}}$. Here, ρ_p is the density of particle, and d_p is the diameter of particle. $\boldsymbol{g}$ is the gravity vector.

Impact and rebound phenomenon of particles

There are three particle–wall collision models. The first one takes the normal and tangential restitution coefficient as constants. The second one takes the normal and tangential restitution coefficient as a function of particle incident angle[2,24] characterized by experiments. The third one is based on the particle impulse and momentum equations set up by experiments.[25,26] In present work, the second particle–wall collision model is used.[24] The impact restitution ratios in the normal and tangential direction to the tube wall are:

$$\frac{V_\mathrm{n2}}{V_\mathrm{n1}} = 1.0 - 0.4159\beta_1 - 0.4994\beta_1^2 + 0.292\beta_1^3 \tag{6}$$

$$\frac{V_\mathrm{t2}}{V_\mathrm{t1}} = 1.0 - 2.12\beta_1 + 3.0775\beta_1^2 - 1.1\beta_1^3 \tag{7}$$

where V_n and V_t represent the particle velocity impact components normal and tangential to the tube wall, respectively. Subscripts 1 and 2 refer to the condition before and after impact, respectively. β_1 is the angle between the incident velocity and the tangent to the surface.

Model for tube mass erosion

There are many models for predicting the erosion rate. Meng et al.[27] summarized 28 kinds of the wear models set up by 1990. Some new models can be found in the recent work.[28] Tabakoff et al.[2] proposed an empirical correlation for estimating the erosion rate of coal ash particles impacting on a steel surface. The erosion mass parameter E is defined as the ratio of the mass loss (milligram) of the target to the mass of the impacting particles (gram),

$$E = K_1 \left\{ 1 + C_\mathrm{K} \left[K_2 \sin\left(\frac{90}{\beta_\mathbf{0}} \beta_1 \right) \right] \right\}^2 V_\mathrm{i}^2 \cos^2 \beta_1 \cdot (1 - R_1^2) + K_3 (V_\mathrm{i}^2 \sin \beta_1)^4 \tag{8}$$

where V_i is the impact velocity, $R_1 = 1 - 0.0016 V_i \sin \beta_1$, β_0 is the angle of maximum erosion. For AISI 304 stainless steel, the angle of maximum erosion is approximately 25° ($\beta_0 \approx 25°$) from the experimental results of Tabakoff et al.[2] $C_K = 1$ for $\beta_1 \leq 3\beta_0$ and $C_K = 0$ for $\beta_1 > 3\beta_0$. K_1, K_2, and K_3 are empirical constants and for coal ash particles impacting on a steel surface, they are $K_1 = 1.505101 \times 10^{-6}$, $K_2 = 0.296007$, and $K_3 = 5.0 \times 10^{-12}$.

Numerical Results and Discussion

The following computational parameters are used in present work: inlet flow velocity $U = 1$ m/s, air density $\rho_\mathrm{f} = 1.2$ kg/m^3, air viscosity $\mu = 1.8 \times 10^{-5}$ kg/(m·s), and particle density $\rho_\mathrm{p} = 2450$ kg/m^3. The tube Reynolds number is $\mathrm{Re_D} = 2 \times 10^3$ based on the tube diameter. The duct Reynolds number is $\mathrm{Re_{Ly}} = 4.2 \times 10^4$ based on cross section length of the duct. The diameter of particle is $d_\mathrm{p} = 6.2$, 20, 80, 200 μm and the corresponding Stokes number is 0.01, 0.1, 1.6, and 10. In present work, the diameter of tube is taken as the characteristic length $\tilde{L} = 30$ mm. The inlet flow velocity is taken as the characteristic velocity $\tilde{U} = 1$ m/s. The characteristic time is $\tilde{t} = \tilde{L}/\tilde{U} = 0.03$ s. The

Table 1. Summary of Prediction Conditions

Parameter	Prediction Values
Free stream pressure, p_∞ (Pa)	1.016×10^5
Free stream temperature, T_∞ (K)	293
Air density, ρ_f (kg/m^3)	1.205
Air viscosity, μ (kg/m/s)	1.8×10^{-5}
Free stream velocity, U(m/s)	1
Tube diameter, D(mm)	30
Tube material	AISI 304 stainless steel
Particle material	Coal ash particle
Particle material density, ρ_p (kg/m^3)	2450
Particle diameter, d_p (μm)	6.2, 20, 80, 200

characteristic density is $\tilde{\rho} = \rho_f = 1.2$ kg/m^3. The characteristic pressure is $\tilde{P} = \rho_f \tilde{U}^2$. The characteristic gravity is $\tilde{g} = \tilde{U}^2/\tilde{L} = 33.3$ m/s^2. The turbulent time scale is the same as the characteristic time is $\tau_f = \tilde{L}/\tilde{U} = 0.03$ s. As the particulate phase is dilute, the volume fraction of the particle phase in all the cases is set as 10^{-4}. Details of the prediction conditions are summarized in Table 1.

Validation

The code of the immersed boundary technique for the simulation of the flow past a stationary tube at low Reynolds number ($Re_D \leq 2 \times 10^2$) was verified by Luo et al.[19] At $Re_D = 1.9 \times 10^3$, the flow past a stationary tube near a wall is calculated and present numerical results are compared with the experimental results of Price et al.[29] The tube center is 1D away from the wall ($G/D = 0.5$ in the case of Price et al.[29]). Three dimensionless mesh sizes are used $h = 1/48$, 1/64, and 1/96 corresponding grids 961 $\times$ 961, 1281 $\times$ 1281, and 1921 $\times$ 1921. The dimensionless time step for the cases of $h = 1/48$ and 1/64 is $\Delta t = 10^{-3}$ and that for $h = 1/96$ is $\Delta t = 5 \times 10^{-4}$. Strouhal number calculated here and obtained experimentally by Price et al.[29] is summarized in Table 2. The relative errors in all simulation cases are below 8% compared with the experimental results.[29] Therefore, it can be concluded that the numerical results are in good agreement with experimental work.

The flow past an aligned tube bank with 10 $\times$ 10 slick tube is simulated. The schematic of the computational domain is shown in Figure 1. Three dimensionless mesh sizes are used $h = 1/48$, 1/64, and 1/96 corresponding grids 1393 $\times$ 1009, 1857 $\times$ 1345, and 2785 $\times$ 2017. The dimensionless time step for the former two cases is $\Delta t = 10^{-3}$ and the last one $\Delta t = 5 \times 10^{-4}$. The dimensionless flow time is defined as $t_{Lx} = L_x/\tilde{U} = 29$. Ten dimensionless flow times are used to collect the statistical time-average pressure calculated through Eq. 9.

$$\frac{p_m}{0.5\rho_f \tilde{U}^2} = \frac{1}{0.5\rho_f \tilde{U}^2 (t_{End} - t_S)} \int_{t_S}^{t_{End}} (p - p_\infty) dt \qquad (9)$$

Table 2. Summary of the Strouhal Number

Authors/Cases	Strouhal Number
Price et al.[29]	0.265
Present, $h = 1/48$, $\Delta t = 10^{-3}$	0.242
Present, $h = 1/64$, $\Delta t = 10^{-3}$	0.245
Present, $h = 1/96$, $\Delta t = 5 \times 10^{-4}$	0.246

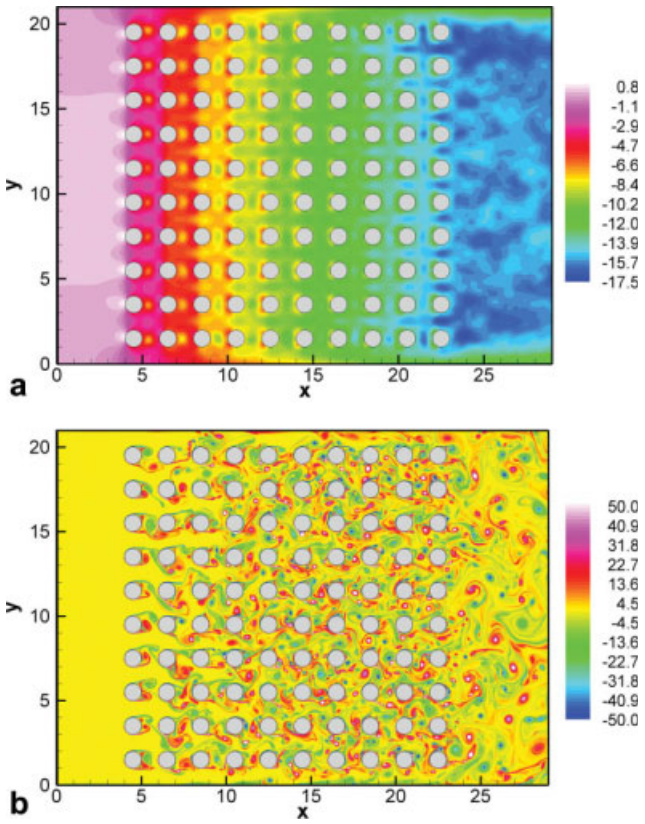

Figure 2. Results of the case of $h = 1/64$ and $\Delta t = 10^{-3}$.

(a) Statistical time-average pressure distribution $p_m/0.5\rho_f \tilde{U}^2$; (b) Instantaneous vortex distribution at dimensionless time $t = 348$. [Color figure can be viewed in the online issue, which is available at www.interscience.wiley.com.]

Figure 2a shows the statistical time-average pressure distribution for the case of $h = 1/64$ and $\Delta t = 10^{-3}$. The mean pressure drops between the positions $\boldsymbol{x}_a = (9.5,10.5)$ and $\boldsymbol{x}_b = (17.5,10.5)$, $\boldsymbol{x}_c = (9.5,11.5)$ and $\boldsymbol{x}_d = (17.5,11.5)$ in the streamwise direction are summarized in Table 3. The results of all cases are compared with the experimental correlation of Zhukauskas.[30] It is seen that the simulations agree well with experimental results. The variations of mean pressure drop between the case $h = 1/64$, $\Delta t = 10^{-3}$ and the case $h = 1/96$, $\Delta t = 5 \times 10^{-4}$ are small. The mesh size $h = 1/64$ is fine enough to obtain the grid independent solution. The instantaneous vortex distribution at dimensionless time $t = 12t_{Lx} = 348$ is shown in Figure 2b for $h = 1/64$ and $\Delta t = 10^{-3}$.

On the basis of the above analysis, the mesh size $h = 1/64$ and time step $\Delta t = 10^{-3}$ are chosen in the present work. The total computational mesh grids are chosen as 1857 $\times$ 1345.

Table 3. Mean Pressure Drop Between Two Positions in Streamwise Direction

Authors/Cases	Mean Pressure Drop $\frac{p_{m,a} - p_{m,b}}{0.5\rho_f \tilde{U}^2}$	Mean Pressure Drop $\frac{p_{m,c} - p_{m,d}}{0.5\rho_f \tilde{U}^2}$
Zhukauskas[30]	4.0	4.0
Present, $h = 1/48$, $\Delta t = 1 \times 10^{-3}$	4.85	4.41
Present, $h = 1/64$, $\Delta t = 1 \times 10^{-3}$	4.62	3.75
Present, $h = 1/96$, $\Delta t = 5 \times 10^{-4}$	4.55	3.71

The statistics for the erosion starts at the second flow time $t_s = 2t_{Lx} = 58$ and ends at the twelfth flow time $t_{\mathrm{End}} = 12t_{Lx} = 348$. Thousand eight hundred particles are released uniformly at the inlet boundary at every 0.2 time period. Totally 3.132×10^6 particles are calculated in the 12 flow time, and 2.61×10^6 particles are used to get the statistical averaging for erosion during the 10 flow time $t_{\mathrm{S}} \approx t_{\mathrm{End}}$. The concept of computational particle[31] is used for two-way coupling to let the volume fraction of the particle phase equal 10^{-4}. A computational particle represents a group of real particles with the same position and velocity. The arrival of one computational particle at the position is equivalent to the arrival of a number of real particles.[31] The code applied in present work for calculating particles trajectories including two-way coupling has been used by Fan et al.[32,33] and Yan et al.[34]

Parameters definition

Local wall collision frequency $\eta_W(x)$ is defined as the number of particles impacting the wall surface of the duct per unit wall length per unit time over the number of particles initially moving into the duct per unit length per unit time. The local wall erosion $Er_W(x)$ is defined as the erosion mass of the wall surface of the duct per unit wall length per unit time over the mass of particles initially moving into the duct per unit length per unit time. The formulation of calculating the local wall erosion at wall surface $\Delta x \in [x_a, x_b]$ is:

$$\int_{x_a}^{x_b} Er_{\mathrm{W}}(x)dx = \int_{x_a}^{x_b} E_{\mathrm{W}}(x)dx \cdot \int_{x_a}^{x_b} \eta_{\mathrm{W}}(x)dx \qquad (10)$$

where $E_{\mathrm{W}}(x)$ is the local wall mass erosion rate (defined in Eq. 8) per unit length of the side walls.

Local tube collision frequency $\eta(\theta)$ is defined as the ratio of the number of particles impacting the tube surface per unit tube angle θ per unit time to the number of particles initially aimed at along the tube surface per unit time. In addition, there are two parameters proposed to evaluate the magnitudes of tube erosion, global tube erosion Er_{G} and local tube erosion $Er(\theta)$. The global tube erosion Er_{G} is defined as the erosion mass of the whole tube surface per unit time over the total mass of particles initially aimed at along the tube surface per unit time. The local tube erosion $Er(\theta)$ is defined as the erosion mass of the tube surface per unit tube angle θ per unit time over the mass of particles initially aimed at along the tube surface per unit time. The relations for the global tube erosion and the local tube erosion are:

$$Er_{\mathrm{G}} = \int_0^{2\pi} Er(\theta)d\theta \qquad (11)$$

And for $\Delta\theta \in [\theta_a, \theta_b]$

$$\int_{\theta_a}^{\theta_b} Er(\theta)d\theta = \int_{\theta_a}^{\theta_b} E(\theta)d\theta \cdot \int_{\theta_a}^{\theta_b} \eta(\theta)d\theta \qquad (12)$$

where $E(\theta)$ is the local tube mass erosion rate (defined in Eq. 8) per unit tube angle of tube. The influence from the local impact velocity and local impact angle can be combined to the local mass erosion rate $E(\theta)$ and $E_W(x)$. Then the global tube erosion Er_{G}, the local tube erosion $Er(\theta)$, the local tube mass erosion rate $E(\theta)$ and local tube collision frequency $\eta(\theta)$ are used for the tube erosion analysis. The local wall erosion $Er_{\mathrm{W}}(x)$, the local wall mass erosion rate $E_{\mathrm{W}}(x)$ and local wall collision frequency $\eta_{\mathrm{W}}(x)$ are used for analyzing wall erosion.

Characteristic of particulate distribution

Particle with different Stokes number shows distinct characteristic in gas–solid two-phase flow. When the Stokes number is 0, the particle is able to completely follow the fluid motion as an ideal tracer, while the Stokes number is large the particle will move independently of turbulent eddies.[35] Figure 3 shows the particulate distribution for different sizes (or Stokes numbers) of particles near the upside wall in the pipe. The smallest size of particles with diameter 6.2 μm (St = 0.01) are easily influenced by the fluid motion to follow the movement of eddies shedding from tubes as shown in Figure 3a. As particle size increase, particulate inertia tends to dominate particle behavior. As shown in Figure 3b (Figure 3c) for the distributions of particle 20 μm (80 μm), particles cannot be attracted into the wake region behind the first tube (Tube 1 in Figure 3b–c). It is quite different from that for the particles with diameter 6.2 μm. The effects of both the particulate inertia and the motion of eddies on large particle trajectories and distributions are less uniform than those for particle 6.2 μm. When the particle size increases to 200 μm, the inertia dominates the movement of particulate motion. As shown in Figure 3d, particles can penetrate the edge of eddy under the effect of inertia, and the distribution of particles becomes more uniform than that for both 20 and 80 μm particles. For 6.2 and 200 μm particles, the distributions are both uniform, but the mechanisms are different. For 200 μm particle, the inertia effect of the particle dominates the particulate motion, but for 6.2 μm particle, the effect of the inertia is very small, and the motion of the fluid dominates the movement of the particle.

Global tube erosion

The particles with different sizes impacting on the same tube can lead to different mass of tube erosion due to different particulate characteristics. On the other hand, the particles with the same size impact on the tubes at different positions can also lead to different mass of tube erosion due to different structure of local flow field. The global tube erosion regarding particle size and tube position is shown in Figure 4. On the first tube (Tube 1 in Figure 3), large-sized particles wear more mass of the tube surface material. However, on the tubes from the second to 10th (Tube 2–10 in Figure 3), 80 μm particles wear the most mass of tube surface material. Compared with the global tube erosion on the first tube, the magnitude of the global tube erosion for 6.2 and 20 μm particles increases at the tubes from the second to the 10th. For 80 and 200 μm particles, the global tube erosions decrease at the second tube but increase for the third to the 10th tube. On the whole 10 tubes, the global tube erosions for 6.2 μm particles are so low that the local tube erosion caused by this size of particles is not worthy of analyzing further in this

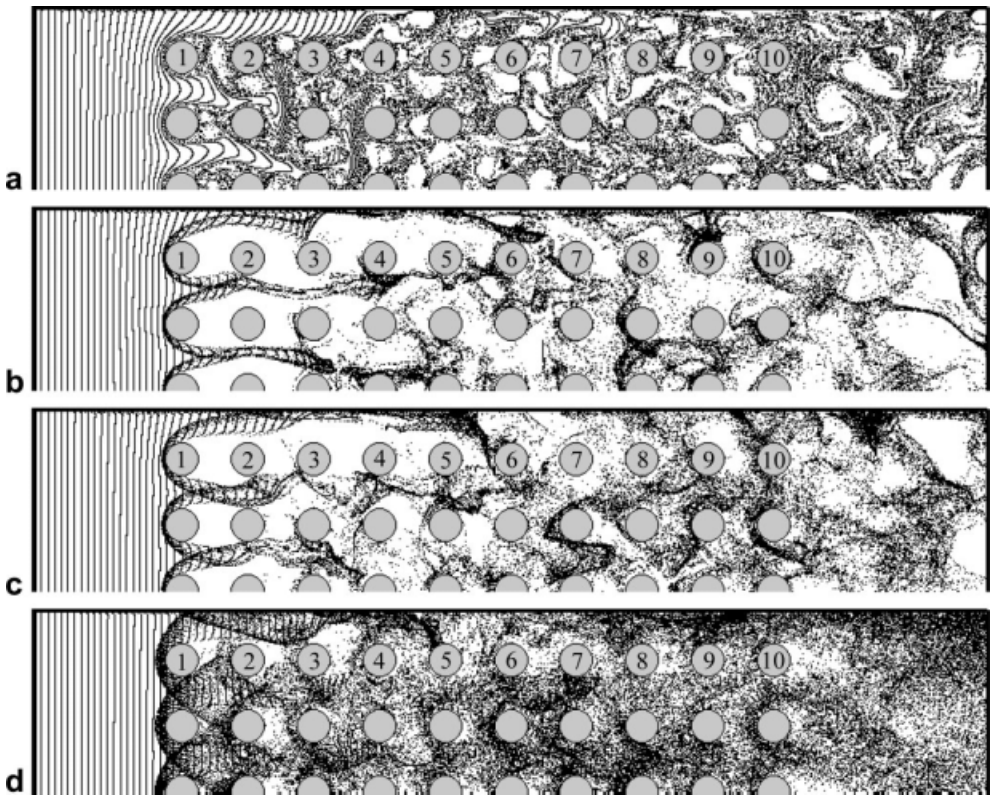

Figure 3. Particulate distributions for different sizes (or Stokes numbers) of particles near the upside wall in the duct (a, b, c and d represent the particles with diameter 6.2, 20, 80, and 200 μm, respectively).

article. For the same reason, the local tube erosion on the first tube caused by 20 μm particles is not analyzed here.

Local tube erosion

As analyzed earlier, it is seen that particles 80, 200 μm are the main abrasives for the first tube (Tube 1 in Figure 1). The local tube erosion on the first tube is shown in Figure 5a. The particles with diameter 80 μm just wear the front side of the first tube ($\theta \in [\pi/2, 3\pi/2]$) while 200 μm particles not only wear the front side but also the back side of this tube. At the front side of this tube, the most erosion of surfaces occurs around $\theta = 2.46$ and 4.07 for 80 μm particles and around $\theta = 2.22$ and 4.13 for 200 μm particles. However, these positions with the largest value of local tube erosion do not have the largest local tube mass erosion rate or local collision frequency. As shown in Figure 5b, the positions with the largest value of local tube mass erosion rate for 80 μm particles are around $\theta = 2.36$ and 4.13 and for 200 μm particles around $\theta = 2.14$ and 4.24. As shown in Figure 5c, there is only one peak for the local collision frequency that is $\theta = 3.25$ for 80 μm particles and $\theta = 3.18$ for 200 μm particles.

The local tube mass erosion rate of the first tube for 80 and 200 μm particles is about $E \sim O(10^{-7})$ mg/g when the inlet flow velocity is $U = 1$ m/s (shown in Figure 5b). The erosion of the tube is proportional to the free stream velocity to the power around 3.0, i.e., $E \propto U^3$. When the inlet flow velocity is 10 m/s, the local tube erosion reaches $E \sim O(10^{-4})$ mg/g, which agrees well with the experimental results of Raask[36] and the numerical results of Fan et al.[7]

At the back side of the first tube, the erosion caused by 200 μm particles occurs around $\theta = 4.94$. The position distribution for 200 μm particles near the first tube is shown in Figure 3d. These 200 μm particles hit and rebound back from the front side of the first tube and move forward under the influence of fluid motion and then impact on the back side of the

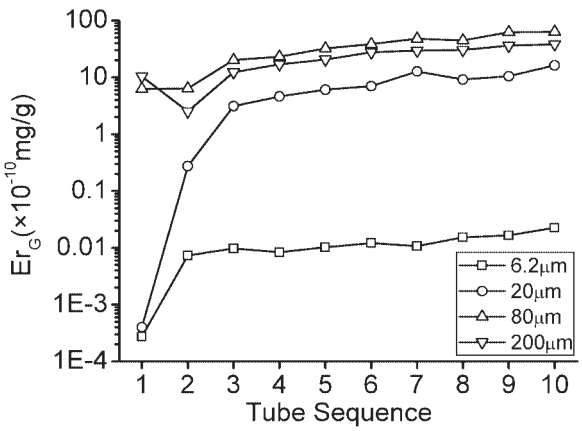

Figure 4. Global tube erosion for different sizes of particles and different positions of tubes.

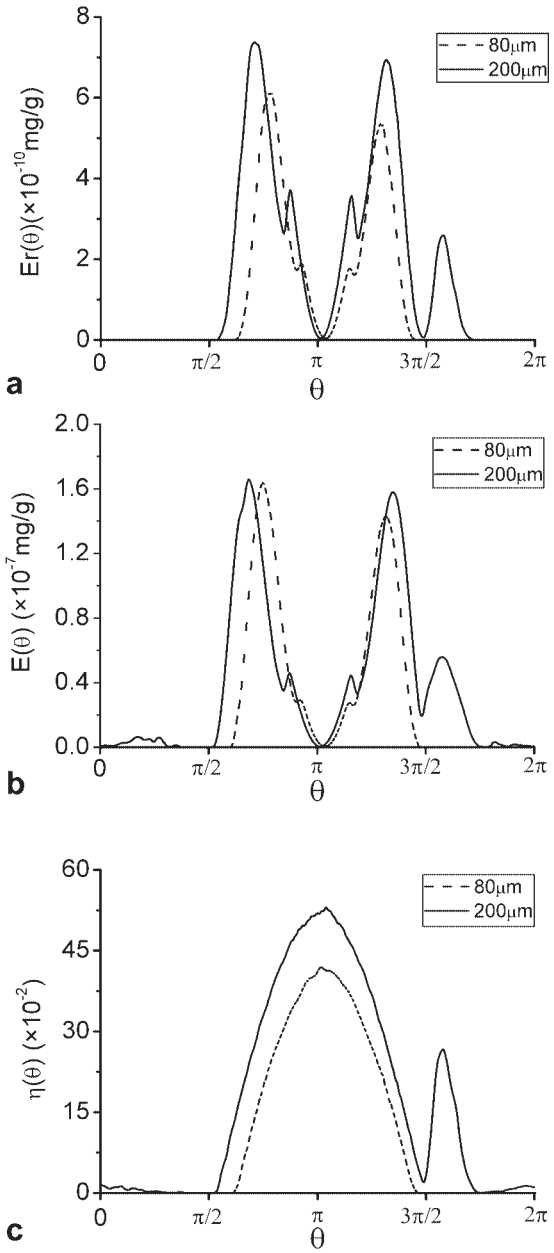

Figure 5. Distribution of (a) local tube erosion, (b) local tube mass erosion rate, and (c) local collision frequency for the first tube.

tube at its neighbor side in transverse direction. Due to the first tube being near the upside wall, only one side of the back side of this tube is eroded by 200 μm particles as shown in Figure 5.

For the second tube (Tube 2 in Figure 1), the main abrasives are the particles with diameter 80 and 200 μm but the erosion caused by 20 μm particles cannot be ignored anymore. Figure 6a shows the local tube erosion on the second tube caused by these three particles. The particles with diameter 80 μm erode the most mass of tube surface material in comparison with other particles. The main erosion of tube occurs at $\theta \in [3.81,4.84]$ and the most erosion does happen around $\theta = 4.44$. For 200 μm particles, the magnitude of the local tube erosion becomes smaller than that of 80 μm particles. On the second tube, there are two wear peaks around $\theta = 2.80$ and 4.40 in the region $\theta \in [2.39,5.37]$. Because this tube is near the upside wall, the damage caused by 200 μm particles around $\theta = 4.40$ is larger than that around $\theta = 2.80$. However, for 20 μm particles, the magnitude of local tube erosion is relatively small as shown in Figure 6a. The local collision frequency at $\theta \in [2.80,3.82]$ for 20 μm particles is very high (shown in Figure 6c), but the local tube mass erosion rate is very low (shown in Figure 6b). The positions of local tube erosion caused by 20 μm particles are mainly at $\theta \in [3.11,4.33]$ with two peaks around

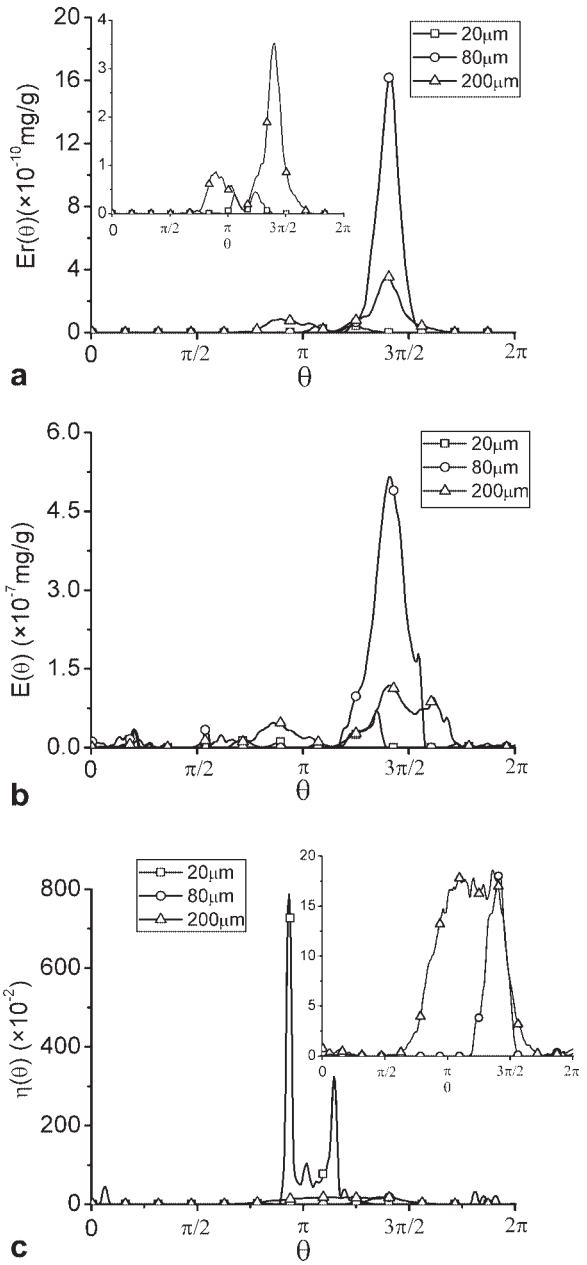

Figure 6. Distribution of (a) local tube erosion, (b) local tube mass erosion rate, and (c) local collision frequency for the second tube.

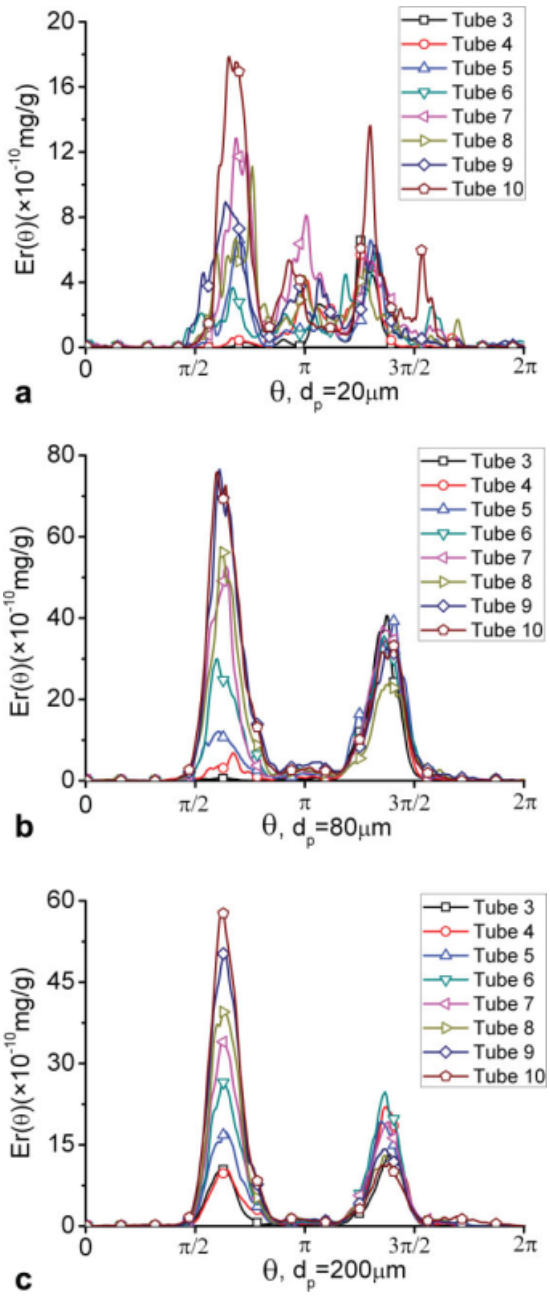

Figure 7. Local tube erosion distribution on the third to the 10th tube (a, b, and c represent the erosion caused by particles with diameter 20, 80, and 200 μm, respectively).

[Color figure can be viewed in the online issue, which is available at www.interscience.wiley.com.]

$\theta = 3.33$ and 3.89 and the magnitudes of the two peaks are relative smaller than those of heavier particles as shown in Figure 6a. In addition, it can be seen that the positions of one peak of local tube erosion for the particles with diameter 80 and 200 μm are almost the same saying that the surfaces of this tube around $\theta = 4.40$ are damaged the most badly.

For the third to the 10th tube (Tube 3–10 in Figure 1), the local tube erosions caused by particles 20, 80, 200 μm are shown in Figure 7. Under the influence of the unstable vortex shedding from the front two tubes, the flow field among these tubes becomes chaotic with lots of eddies. Motion of particles as small as 20 μm will be affected by turbulent eddies so that the local collision frequency at these tubes is much different from that for large particles as shown in Figure 9a. For 20 μm particles, these positions of tube around $\theta = 0.45$, 1.36, 3.37, and 5.41 are suffered more particulate impingement. The local tube mass erosion rate for 20 μm

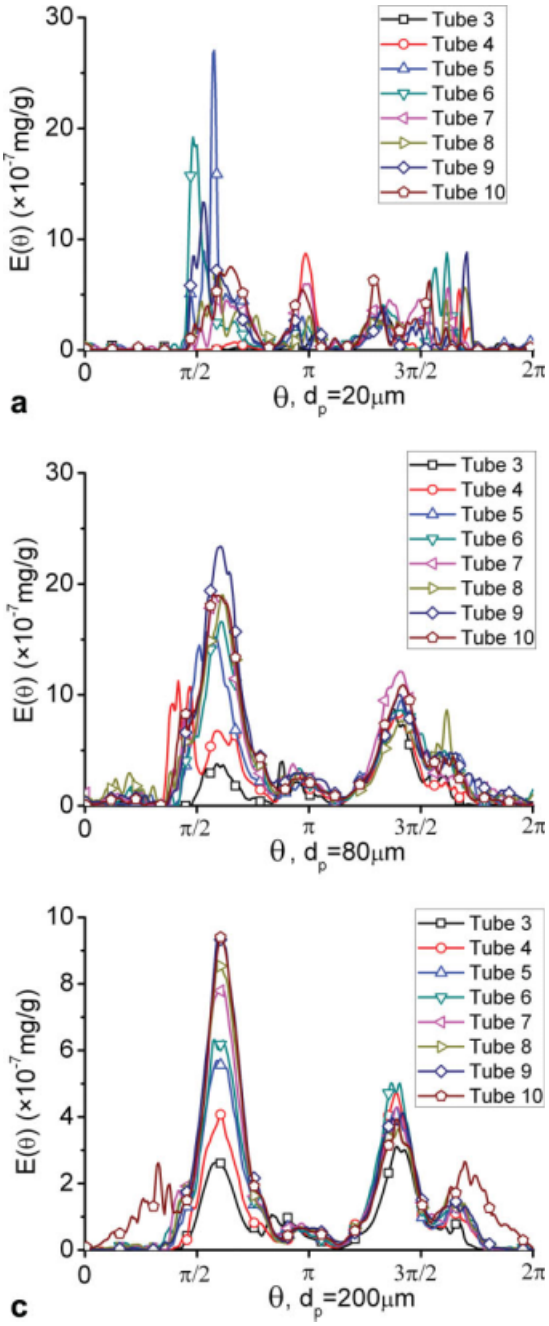

Figure 8. Local tube mass erosion rate distribution on the third to the 10th tube (a, b, and c represent the erosion caused by particles with diameter 20, 80, and 200 μm, respectively).

[Color figure can be viewed in the online issue, which is available at www.interscience.wiley.com.]

particles occurs mainly around $\theta = 1.81$, 3.10, 4.05, and 5.13 as shown in Figure 8a. In Figure 7a, it can be seen that the local tube erosion on these seven tubes occurs at the position $\theta \in [1.41,5.39]$ with three peaks around $\theta = 2.11$, 3.16, and 4.07 at the front side of tubes and one peak around $\theta = 4.83$ at the back side of these tubes.

As particle size increases, the inertia effect does more effect on the trajectories of particles. Figure 7b shows the local tube erosion for the particles with diameter 80 μm on the tubes from the third to 10th. It is seen that the positions of local tube erosions are very close mainly at $\theta \in [1.38,2.70] \cup [3.61,4.93]$ with two peaks around $\theta = 1.95$ and 4.37. Because of these tubes near the upside wall of the duct, the characteristics of the local tube erosion at the upside surfaces of these tubes $\theta \in [0,\pi]$ are quite different from those of that at the downside surfaces of these tubes $\theta \in [\pi,2\pi]$. At the downside surfaces of these seven tubes, the maximum local tube erosion are almost the same because the local tube mass erosion rates (shown in Figure 8b) and the local collision frequencies (shown in Figure 9b) in these regions are almost the same. However, at the upside surfaces, the maximum local tube erosion increases with the sequence number of the tube. Figure 7c shows the seven tubes erosion for 200 μm particle. The curves of the local tube erosion on each tube are very similar as well as the same places $\theta \in [1.34,2.65] \cup [3.70,4.78]$ with two peaks around $\theta = 1.94$ and 4.28. The characteristics of local tube erosion at the upside/downside surface of tube are almost the same as those for 80 μm particles. That the similarities of the local tube mass erosion rates (shown in Figure 8c) and local collision frequencies (shown in Figure 9c) leads to the similar maximum local tube erosion and similar erosion positions at the downside surfaces of these seven tubes. At the upside surfaces of these tubes, similarly, the maximum value of local tube erosion increases with the sequence number of the tube. This is due to the fact that the maximum values of local tube mass erosion rate (shown in Figure 8c) and local collision frequency (shown in Figure 9c) at this region of these seven tubes increase with the sequence number of tubes. Therefore, near a sidewall, on the tubes lain from the third to 10th (Tube 3–10 in Figure 1), particles with large sizes (80 and 200 μm) wear almost the same places of the tubes' surfaces around $\theta = 1.95$ and 4.30. The maximum local tube erosion at the downside surfaces of these seven tubes are almost the same while that increases with the sequence number of the tube at the upside surfaces.

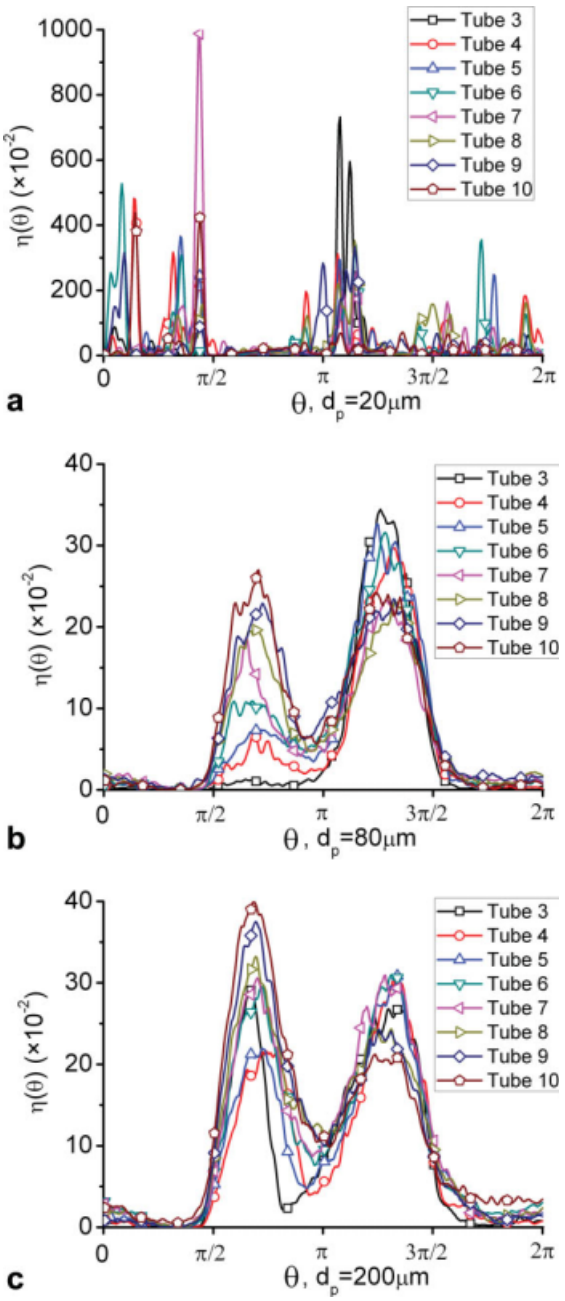

Figure 9. Local tube collision frequency distribution on the third to the 10th tube (a, b, and c represent the erosion caused by particles with diameter 20, 80, and 200 μm, respectively).

Side wall erosion

When particles pass an aligned tube bank in a duct, these particles not only wear tubes but also erode the side walls of the duct. Heavy particles can penetrate the eddies with the inertia effect and impact on the side walls directly while light particles are carried by eddies and impact on the side walls when these carrier eddies contact the side walls.

Figure 10 shows the local wall collision frequency which is the average value of the upside and downside walls for different sized particles. The position in front of the first tube $x \in [0,4.5]$ is suffered a large number of particle impingements. The starting point at the side walls for particle collision are $x = 1.42$, 1.48, 2.05, and 3.15 for the abrasive particles with diameter 6.2, 20, 80, and 200 μm, respectively. The local wall collision frequencies for all the large and small size particles decrease rapidly at the position before the first tube in the streamwise direction. At the position $x \in [4.5,22.5]$, the local wall collision frequency for small particles with diameter 6.2 μm is the highest one while that for 80 μm particles is the smallest. Light particles impact on the side walls more easily than heavy particles when the flow field is chaotic.

Figure 11 shows the local wall mass erosion rate which is the average value of the upside and downside walls for

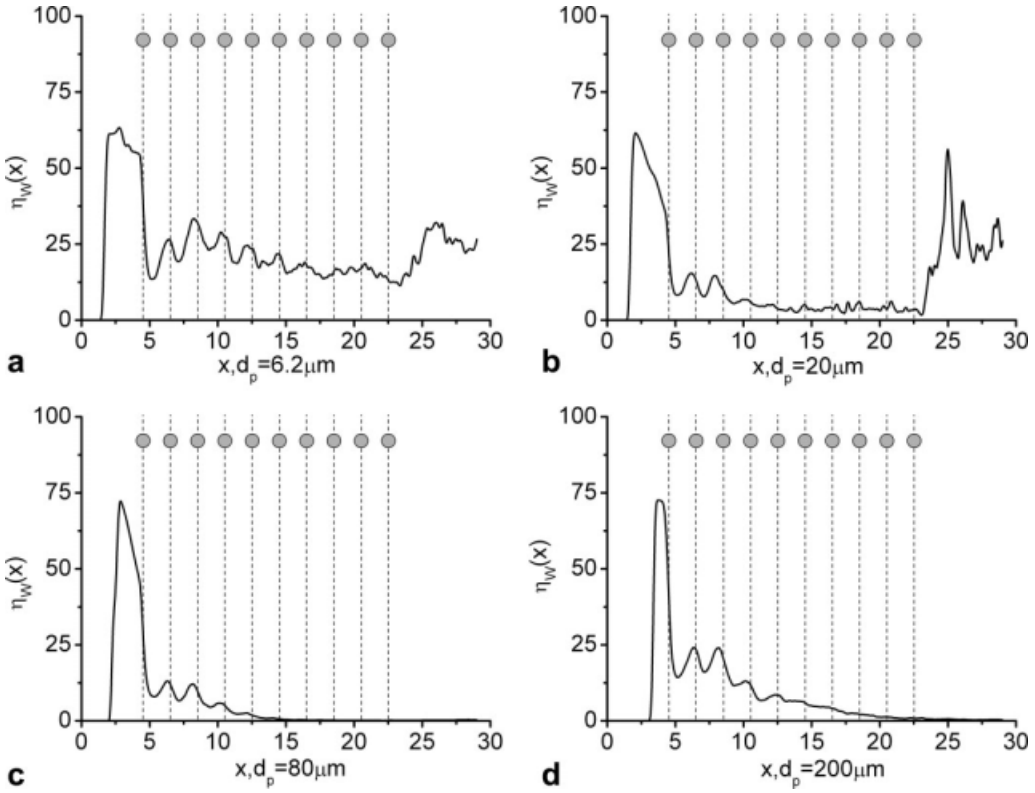

Figure 10. Local wall collision frequency distribution (a, b, c, and d represent the erosion caused by particles with diameter 6.2, 20, 80, and 200 μm, respectively).

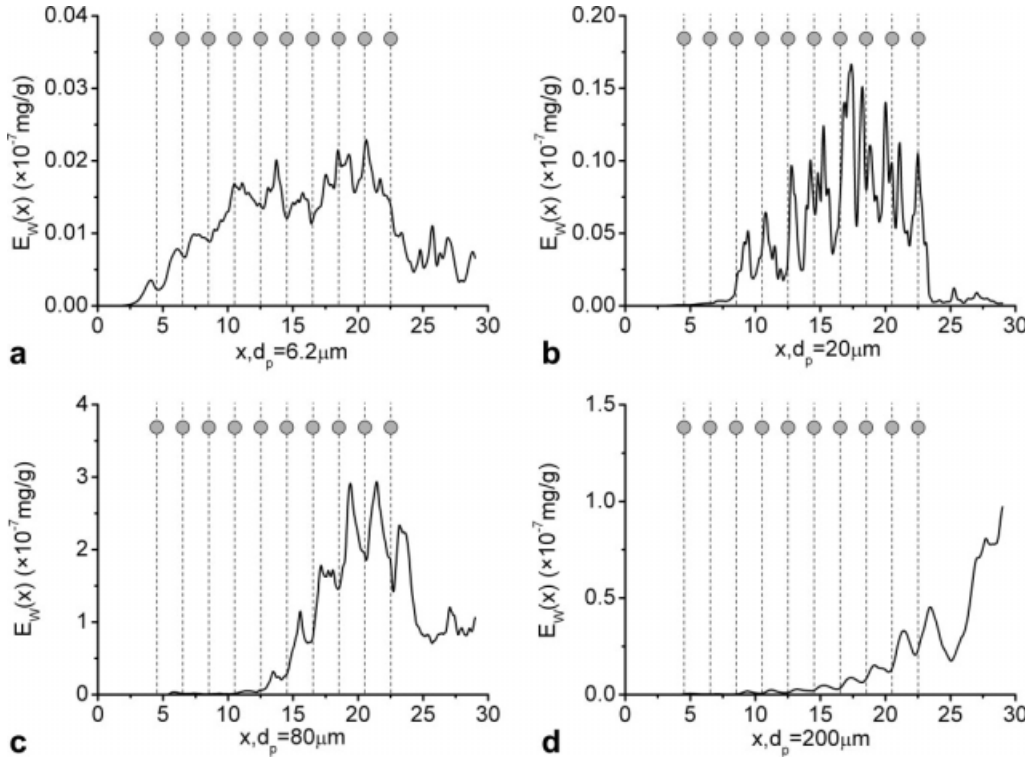

Figure 11. Local wall mass erosion rate distribution (a, b, c, and d represent the erosion caused by particles with diameter 6.2, 20, 80, and 200 μm, respectively).

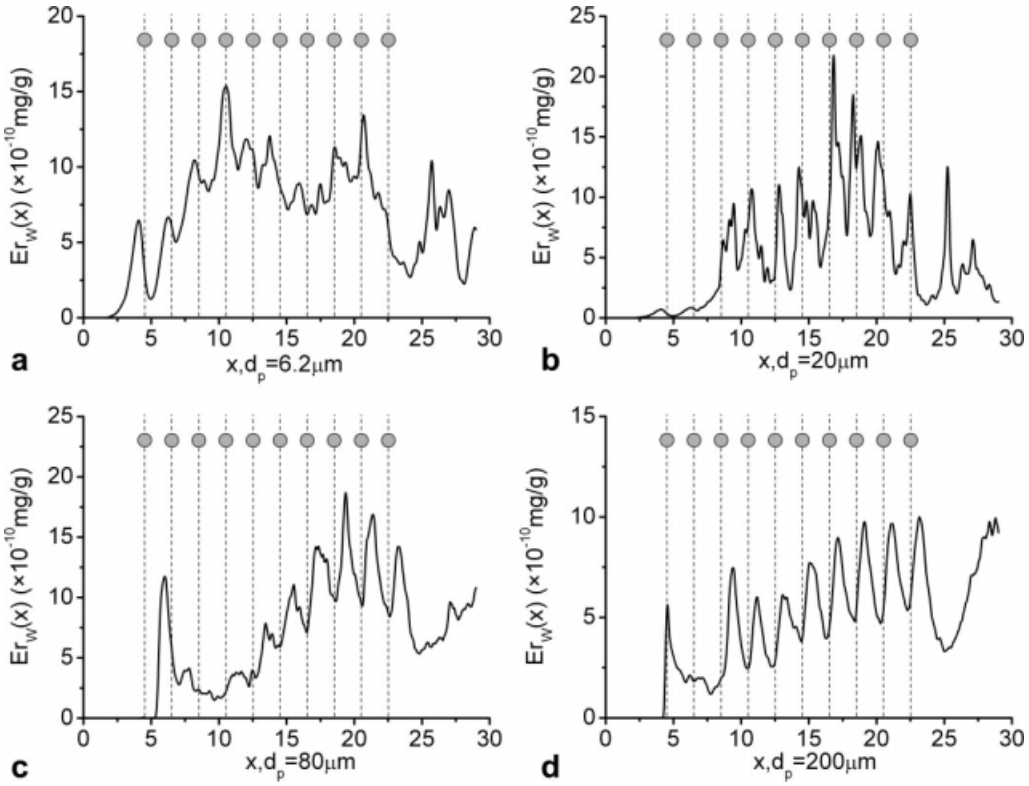

Figure 12. Local wall erosion distribution (a, b, c, and d represent the erosion caused by particles with diameter 6.2, 20, 80, and 200 μm, respectively).

different sized particles. For the 6.2 μm particle, the starting point at the side wall for local wall mass erosion rate is $x = 2.35$ which is in front of the first tube. As particles size increases, the position of the starting point for local wall mass erosion rate moves in the downstream direction. The local wall mass erosion rate increases significantly at the positions $x = 8.50$, 12.50, 14.50 for the particles with diameter 20, 80, and 200 μm, respectively.

The magnitude of the local wall mass erosion rate and the local wall collision frequency determines the magnitude of local wall erosion. High local wall erosion occurs where there is high wall mass erosion rate and high local wall collision frequency. On the other hand, the positions with only a large value of local wall mass erosion rate or with only a large value of local wall collision frequency are not always the positions with large values of local wall erosion. As shown in Figure 12, the magnitudes of local wall erosion for all the four sizes of particles are very close. For the smallest size of particle with diameter 6.2 μm, high local wall collision frequency increases the magnitude of eroded mass of the side wall material. For 80 μm particles, the higher local wall mass erosion rate leads to more mass of side wall material be eroded.

The positions where the local wall erosion start at the side wall are $x = 1.80$, 2.70, 5.33, and 4.20 for particles with diameters 6.2, 20, 80, and 200 μm, respectively. For 20 μm particles, though the starting point of wall erosion by particles is at $x = 2.70$, the value of local wall erosion increases significantly at $x = 8.35$ which is around the location of the third tube. While for the other size particles (6.2, 80, and 200 μm), the local wall erosion increases rapidly from the starting point where the wall starts to be eroded by particles.

Conclusions

CFD tool has been used to simulate particulate flows past a 10×10 aligned tube bank and particularly study the erosion of duct side wall and that of tubes near the duct wall due to particle-wall impaction. Coal ash particles with diameter 6.2, 20, 80, and 200 μm are used as the abrasives. The tube erosion and side wall erosion are analyzed and some features are captured. The conclusions arising from present investigation can be summarized as follows.

(1) The erosion of the first tube in the streamwise direction increases with particle size. For the tubes from the second to the 10th, 80 μm particle causes the highest erosion while 6.2 μm particle does the lowest.

(2) Particle with size of 20 μm can collide on the both sides of the tubes from the third to the 10th. However, the tube erosion caused by these particles occurs mainly at the front side of these tubes.

(3) Large particles, i.e., 80, 200 μm, wear almost the same places of the third to 10th tubes' surfaces around $\theta = 1.95$ and 4.30. The maximum erosion of these tubes (third to 10th) increases with the sequence number of the tube.

(4) The magnitudes of local wall erosion caused by all four sized particles are very close. For the 6.2 μm particle,

chaotic eddies near the side wall increase the local wall collision frequency and then augments the wall erosion. For the heavy particles, the increment of the local wall mass erosion rate leads to increase the wall erosion.

Acknowledgments

This work is supported by the National Natural Science Foundation of China (No. 50736006, No. 50776080). We are grateful to that.

Notation

c = mean velocity at the outflow boundary in Eq. 4
C_K = material wear constant
D = tube diameter, mm
d_p = particle diameter, μm
E = erosion parameter, mg/g
Er = local erosion, mg/g
Er_G = global tube erosion, mg/g
F_k = dimensionless force exerted on the kth Lagrangian point
f = external force in Eq. 2
f_d = two phase coupling term
f_p = modified factor of the Stokes drag force in Eq. 5
G = Gap between the tube and the wall
$\boldsymbol{g}$ = dimensionless gravity
h = dimensionless grid size
K_1, K_2, K_3 = material constants in Eq. 8
L = characteristic length of flow field, m
L_x = computational length in streamwise direction
L_y = computational length in transverse direction
P = dimensionless pressure
p = fluid pressure, Pa
p_∞ = free stream pressure, Pa
R_1 = temporary parameter in Eq. 8
Re = Reynolds number
Re_D = tube Reynolds number
Re_{Ly} = duct Reynolds number
Re_p = particle Reynolds number
St = Stokes number
T_∞ = free stream temperature, K
t = dimensionless time
t_{Lx} = dimensionless flow time
U = velocity of flow field, m/s
$\boldsymbol{u}$ = dimensionless fluid velocity vector
$\boldsymbol{V}$ = dimensionless particle velocity vector
$\boldsymbol{x}$ = dimensionless position vector of Eulerian mesh
$\boldsymbol{x}_k$ = dimensionless position vector of the kth Lagrangian point

Greek letters

Ω = whole computational domain
ρ_f = fluid density, kg/m^3
ρ_p = particle density, kg/m^3
μ = fluid viscosity, kg/(m·s)
δ = dirac delta function
β_0 = angle of maximum erosion
β_1 = relative angle between particle path and tube surface
θ = tube angle, arc
η = local collision frequency
Δt = dimensionless time step
τ_f = turbulent time scale, s

Superscript

$\sim$ = characteristic parameter

Subscript

a,b,c,d = parameters for distinguishing different locations
i = particle impact parameter
m = mean value
n = normal component
S = start time of statistics
End = end time of statistics
W = wall parameter
t = tangential component
1 = conditions of the particle approaching towards the tube
2 = conditions of the particle rebounding from the tube

Literature Cited

1. Finnie I. Erosion of surfaces by solid particles. *Wear*. 1960;3:87–103.
2. Tabakoff W, Kotwal R, Hamed A. Erosion study of different matericals affected by coal ash particles. *Wear*. 1979;52:161–173.
3. Laitone JA. Aerodynamic effects in the erosion process. *Wear*. 1979;56:239–246.
4. Sundararajan G. An empirical relation for the volume of the crater formed during high velocity oblique impact tests. *Wear*. 1984;97:9–16.
5. Deng T, Bingley MS, Bradley MSA. The influence of particle rotation on the solid particle erosion rate of metals. *Wear*. 2004;256:1037–1049.
6. Lee B, Fletcher CAJ, Behnia M. Computational study of solid particle erosion for a single tube in cross flow. *Wear*. 2000;240:95–99.
7. Fan JR, Zhou DD, Jin J, Cen KF. Numerical simulation of the tube erosion by particle impaction. *Wear*. 1991;142:171–184.
8. Sato S, Shimizu A, Yokomine T. Numerical prediction of erosion for suspension flow duct. *Wear*. 1995;186–187:203–209.
9. Wallace MS, Dempster WM, Scanlon T, Peters J, McCulloch S. Prediction of impact erosion in valve geometries. *Wear*. 2004;256:927–936.
10. Fan JR, Zhou DD, Zeng KL, Cen KF. Numerical and experimental study of finned tube erosion protection methods. *Wear*. 1992;152:1–19.
11. Song XQ, Lin JZ, Zhao JF, Shen TY. Research on reducing erosion by adding ribs on the wall in particulate two-phase flows. *Wear*. 1996;193:1–7.
12. Fan JR, Luo K, Zhang XY, Cen KF. Large eddy simulation of the anti-erosion characteristics of the ribbed-bend in gas-solid flows. *J Eng Gas Turbines Power, ASME Trans*. 2004;126:672–679.
13. Mbabazi JG, Sheer TJ. Computational prediction of erosion of air heater elements by fly ash particles. *Wear*. 2006;261:1322–1336.
14. Sbrizzai F, Lavezzo V, Verzicco R, Compolo M, Soldati A. Direct numerical simulation of turbulent particle dispersion in an unbaffled stirred-tank reactor. *Chem Eng Sci*. 2006;61:2843–2851.
15. Gradl J, Schwarzer HC, Schwertfirm F, Manhart M, Peukert W. Precipitation of nanoparticles in a T-mixer: coupling the particle population dynamics with hydrodynamics through direct numerical simulation. *Chem Eng Proc*. 2006;45:908–916.
16. Schuh MJ, Schuler CA, Humphrey JAC. Numerical calculation of particle-laden gas flows past tubes. *AIChE J*. 1989;35:466–480.
17. Peskin CS. The immersed boundary method. *Acta Numerica*. 2002;11:479–517.
18. Wang Z, Fan J, Luo K. Combined multi-direct forcing and immersed boundary method for simulation flows with moving particles. *Int J Multiphase Flow*. 2008;34:283–302.
19. Luo K, Wang Z, Fan J, Cen K. Full-scale solutions to particle-laden flows: multidirect forcing and immersed boundary method. *Phys Rev E*. 72:066709, 2007.
20. Lele SK. Compact finite difference scheme with spectral-like resolution. *J Comput Phys*. 1992;103:16–42.
21. Jameson A, Schmidt W. Some recent development in numerical methods for transonic flow. *Comput Methods Appl Mech Eng*. 1985;51:467–493.
22. Orlanski I. A simple boundary condition for unbounded hyperbolic flow. *J Comput Phys*. 1976;21:251–269.
23. Le H, Moin P, Kim J. Direct numerical simulation of turbulent flow over a backward-facing step. *J Fluid Mech*. 1997;330:349–374.
24. Tabakoff W, Grant G, Ball R. An experimental investigation of certain aerodynamic effects on erosion. *AIAA Paper*. 1974;74–639.
25. Sommerfeld M. Modeling of particle-wall collisions in confined gas-particle flows. *Int J Multiphase Flow*. 1992;18:905–926.
26. Sommerfeld M, Huber N. Experimental analysis and modeling of particle-wall collisions. *Int J Multiphase Flow*. 1999;25:1457–1489.
27. Meng HC, Ludema KC. Wear models and predictive equations: their form and content. *Wear*. 1995;181–183:443–457.
28. Oka YI, Okamura K, Yoshida T. Practical estimation of erosion damage caused by solid particle impact. Part 1: effects of impact parameters on a predictive equation. *Wear*. 2005;259:95–101.

29. Price SJ, Sumner D, Smith JG, Leong K, Païdoussis MP. Flow visualization around a circular cylinder near to a plane wall. *J Fluids Struct*. 2002;16:175–191.
30. Zhukauskas A. *Heat Transfer from Tubes in Cross Flow. Advances in Heat Transfer*, Vol. 8. New York: Academic Press, 1972:93–106.
31. Elghobashi S. On predicting particle-laden turbulent flows. *Appl Sci Res*. 1994;52:309–329.
32. Fan J, Luo K, Zheng Y, Jin H, Cen K. Modulation on coherent vortex structures by dispersed solid particles in a three-dimensional mixing layer. *Phys Rev E*. 2003;68:036309.
33. Fan J, Luo K, Ha MY, Cen K. Direct numerical simulation of a near-field particle-laden plane turbulent jet. *Phys Rev E*. 2004;70:026303.
34. Yan J, Luo K, Fan J, Tsuji Y, Cen K. Direct numerical simulation of particle dispersion in a turbulent jet considering inter-particle collisions. *Int J Multiphase Flow*. 2008;34:723–733.
35. Yamamoto Y, Potthoff M, Tanka T, Kajishima T, Tsuji Y. Large-eddy simulation of turbulent gas-particle flow in a vertical channel: effect of considering inter-particle collisions. *J Fluid Mech*. 2001;442:303–334.
36. Raask E. Tube erosion by ash impaction. *Wear*. 1969;13:301–315.

Manuscript received July 13, 2008, and revision received Apr. 30, 2009.